*Bangladesh Journal of Physics, Vol. **31**, Issue 1, pp. 17–41, June 2024*

EXPLORING THE IMPACT OF Mg CONTENT ON THE STRUCTURAL, MORPHOLOGICAL, AND OPTICAL CHARACTERISTICS OF HYDROTHERMALLY SYNTHESIZED Mg-DOPED α-MoO_3 NANOBELTS

K. HOQUE[1,*], P. MONDAL[1], M. S. MANIR[2], S. DUTTA[3], P. BALA[4], S. K. SEN[5]

[1]*Physics Discipline, Khulna University, Khulna, Bangladesh*

[2]*Institute of Radiation and Polymer Technology, AERE, Bangladesh Atomic Energy Commission, Dhaka, Bangladesh*

[3]*Ministry of Education, Government of the People's Republic of Bangladesh, Dhaka, Bangladesh*

[4]*Department of Physics, Jagannath University, Dhaka, Bangladesh*

[5]*Institute of Electronics, Atomic Energy Research Establishment, Bangladesh Atomic Energy Commission, Dhaka, Bangladesh*

[*]*Corresponding author e-mail: hoquekarimul@phy.ku.ac.bd*

Received on 21.04.2024, Revised received on 09.05.2024, Accepted for publication on 10.05.2024

DOI: *https://doi.org/10.3329/bjphy.v31i1.79517*

ABSTRACT

This study focused on synthesizing Mg-doped (0, 2, 4 & 6 mol% Mg) molybdenum oxide (MoO_3) with a stable crystal structure using the hydrothermal method. X-ray diffraction (XRD) analysis verified the exclusive presence of the orthorhombic phase, free from any combined phases or contaminants. The Williamson-Hall, Halder-Wagner, and Scherer techniques were employed to assess crystallite dimensions and lattice strains. Microstructural parameters, such as dislocation density and lattice parameters, were calculated. FTIR characterization and vibrational behavior of chemical bonds confirmed α-MoO_3 formation. SEM images verified a nanobelt structure with random distribution in both undoped and Mg-doped α-MoO_3, and revealed that their lengths and widths ranged from 1.493 to 1.784 m and 157 to 252 nm, respectively. Optical band gaps, determined using UV-visible spectroscopy, ranged from 3.05 to 3.15 eV, decreasing with increased doping. After examination of the SEM and optical properties, we found that factors like shape, size, and crystallinity can influence energy gaps. Employing the energy dispersive X-ray (EDX) method to examine the elemental composition confirmed the presence of oxygen, Mo, and Mg in all doped samples. Our work indicates that Mg-doped α-MoO_3 is a cost-effective iso-valent element that could find applications in processes such as water oxidation and various other photochemical activities.

Keywords: *MoO_3, Hydrothermal synthesis, Nanobelts, XRD, FTIR, SEM, UV-vis spectrophotometer, EDX.*

1. INTRODUCTION

Transition metal oxides (TMO) are increasingly important in nanoscience and technology due to their excellent properties and potential applications, prompting researchers to invest in their synthesis. The nano crystalline TMOs like TiO_2 [1], WO_3 [2], ZnO [3], NiO [4] and MoO_3 [5] have been extensively researched. Within this group, molybdenum trioxide (MoO_3) has garnered significant attention in recent decades due to its exceptional attributes, including strong stability, distinctive quantum size and surface effects, reactivity, association with various valence states, and impressive thermal and chemical stability [6]. An instance of a layered *n*-type metal oxide semiconductor is demonstrated by molybdenum trioxide (MoO3). Typically, it exists in three

primary crystalline forms: the orthorhombic phase (α-MoO_3) which is thermodynamically stable and remaining other two phases are metastable, namely hexagonal (*h*-MoO_3) and monoclinic (β-MoO_3). The distinctive layered structure of the α-MoO_3 phase is created through the corner-sharing arrangement of [MoO_6] octahedrons along the [001] and [100] orientations. By sharing the edges of octahedrons along the [001] direction, two sub-layers are combined. The arrangement of these layers alternately along the [010] direction, facilitated by van der Waals interaction, results in the creation of a two-dimensional structure characteristic of α-MoO_3[7]. Until now, diverse morphologies of α-MoO_3 have been documented, encompassing variations such as nanowires, nanotubes, nanoplates, nanorods, and nanobelts. Notably, the nanostructured α-MoO_3 in the form of belts has garnered significant attention. This interest stems from the singular single-crystalline attributes it holds, which are believed to offer distinctive properties compared to bulk crystals [9]. The crystal structure of β-MoO_3, which exhibits a monoclinic arrangement, differs significantly from that of α-MoO_3. It bears resemblance to the cubic structure of Rhenium trioxide (ReO_3). Within this arrangement, the MoO_6 octahedral entities distribute their corners' oxygen atoms in alignment with the *c*-axis, and they share. In addition to the aforementioned phases, MoO_3 can also adopt a hexagonal configuration (*h*-MoO_3). In this particular phase, the configuration consists of interconnected zigzag chains formed by MoO_6octahedral, which share corners along the *c*-axis. Nano-materials derived from MoO_3 have garnered growing interest across various domains, encompassing applications like antibacterial uses [8], photo-catalysis[9], gas sensing[10], lithium batteries[11], organic solar cells[12], photochromic devices [13], pseudo-capacitors[14],display devices and smart windows [6]. In recent times, researchers have successfully produced nanoparticles using various techniques including chemical vapor deposition [15], co-precipitation [16], sol-gel method [17], spray pyrolysis [18], thermal decomposition [4], thermal evaporation [19], hydrothermal [20]among others. The resulting particle size and morphology are contingent upon the specific synthesis method employed. Among these techniques, the hydrothermal approach stands out as a widely embraced method, offering a solution-based chemical route for synthesizing diverse nanostructured materials. This method has significant advantages, including its capacity to finely adjust the crystal structure (both stable and metastable), size and morphology by manipulating various reaction parameters like reactant source, reaction time, reaction temperature, additives and solvent medium. Additionally, the hydrothermal synthesis method is characterized by its eco-friendly and economical nature, while also providing a remarkable degree of molecular-scale chemical consistency. Consequently, a hydrothermal method mediated by an autoclave has been adopted to selectively and sequentially synthesize stable α-MoO_3 nanocrystals. This thesis work delves into a comprehensive exploration of the impact of experimental variables – such as the choice and quantity of precipitant, reaction time, reactant solvent medium and temperature – on the development of nanobelt structures within MoO_3 nanocrystals. Researchers like A. Chithambararaj et al. in 2011 [21], Xiaofei Yang et al. in 2011 [20], and Yuping Chen et al. in 2010 [22] have successfully employed the hydrothermal technique to synthesize α-MoO_3 nanobelts.

In a perfect scenario, crystals would infinitely extend in all directions, but due to their finite size, no crystals can achieve perfection. This finite size results in a widening of the diffraction peaks. Analyzing this peak broadening provides two key characteristics are lattice strain and crystallite size. Crystallite size quantifies the dimensions of the coherent diffracting domain, while lattice strain gauges the variance in lattice constants due to dislocations lattice imperfections. Various techniques exist for estimating these parameters, including Rietveld refinement, pseudo Voigot function, Warren Averbach analysis, Williamson-Hall analysis, Size-Strain plot analysis and Halder-Wagner analysis. Among these methods, this current study adopts the Williamson-Hall and Halder-Wagner

techniques for simplicity. Williamson-Hall analysis simplifies the integral breadth approach, includes the widening caused by both size and strain effects, depicting the width of the peak as a function of 2θ. Additionally, Scherer's technique is used to compute crystallite size and dislocation density. In the pursuit of enhancing device performance, incorporating metal elements through doping has emerged as a highly effective technique. This approach allows for precise modulation of the optical and electrical characteristics of semiconductors. Within this study, we achieved the synthesis of consistent nanobelts for both undoped and Mg-doped α-MoO_3. An in-depth analysis of the structural, morphological, and optical attributes of these nanobelts was conducted, with a particular focus on understanding the influence of Mg as an impurity.

Some elements have been used for the doping of MoO_3 as Co [23], Dy [7], Ni [24], Ti[25], Zn [26], Er[27], Eu [28], W [29], Ce [30], Cd [31], Ag [32], Fe [33] etc. Similar to various metal oxides, the introduction of rare earth elements are dopants into MoO_3 can augment specific physical characteristics and create avenues for potential applications. This is due to the elevated surface basicity, rapid oxygen ion mobility, and intriguing catalytic attributes associated with rare earth oxides, qualities believed to hold significance in the context of gas sensing applications.

2. EXPERIMENTAL DETAILS

2.1 Materials

Pure and Mg-doped α-MoO_3 nanobelts were synthesized with varying concentrations of Magnesium (2%, 4%, and 6% M) using a straightforward hydrothermal synthesis method under ambient conditions. The precursor material utilized was ammonium heptamolybdate tetrahydrate (AHM), [$(NH_4)_6Mo_7O2_4{\cdot}4H_2O$], obtained from Sigma Aldrich Ltd., USA, with a purity of 99%. To introduce the doping element, Magnesium chloride [$MgC_{l2}{\cdot}6H_2O$] from Sigma Aldrich Ltd., USA, with a purity exceeding 98%, was incorporated into the initial solution. Additional chemicals employed in the nanobelt synthesis encompassed concentrated nitric acid (37% HNO_3) and deionized water. All materials and chemicals employed, sourced from local markets as certified agents, were utilized without further purification.

2.2 Nanobelts Synthesis Procedure

In a standard hydrothermal synthesis process, 6gm of ammonium heptamolybdate tetrahydrate ($(NH_4)_6Mo_7O_{24}{\cdot}4H_2O$) were dissolved in 242.5mm of deionized water. The solution was incessantly stirred for 15 minutes at a speed of 60 revolutions per minute at room temperature. Following this, a certain amount of magnesium chloride hexahydrate ($MgCl_2{\cdot}6H_2O$) was dissolved in the solution at 2% mole ratio. This mixture underwent another 15 minutes of continuous stirring. Subsequently, 24.25mm of concentrated nitric acid (37% HNO_3) were gradually added to the solution while stirring continuously for 15 minutes at room temperature. After completing the above steps, precursor solutions with 4% and 6% magnesium content were prepared separately. These three precursor solutions were then placed into separate stainless-steel autoclaves. The autoclaves were maintained at a temperature of around 135°C for 10hrs duration. After the autoclaves naturally reached room temperature, the formed deposits were gathered using centrifugation. These collected deposits underwent repeated washing with deionized water and absolute ethanol. Eventually, they were subjected to drying at 85°C for 12hrs within a vacuum oven. The next step involved annealing the precipitates in an electric furnace at a temperature of approximately 450°C for a period of 3 hours. This process resulted in the formation of magnesium-doped α-MoO_3 nanobelts. For comparison, a

similar synthesis approach was followed to create pristine α-MoO_3 nanobelts without adding the dopant material, magnesium chloride ($MgCl_2 \cdot 6H_2O$).The reaction formula for the formation of α-MoO_3 is.

$$(NH_4)_6Mo_7O_{24}.4H_2O\,(aq) + 6HNO_3 \rightarrow 7MoO_3\,(s) + 6\,NH_4NO_3\,(aq) + 7H_2O(l)$$

Figure 1 are shows illustrates diagram depicting the hydrothermal synthesis process described earlier for both unmodified α-MoO_3 nanobelts and α-MoO_3 nanobelts doped with Mg.

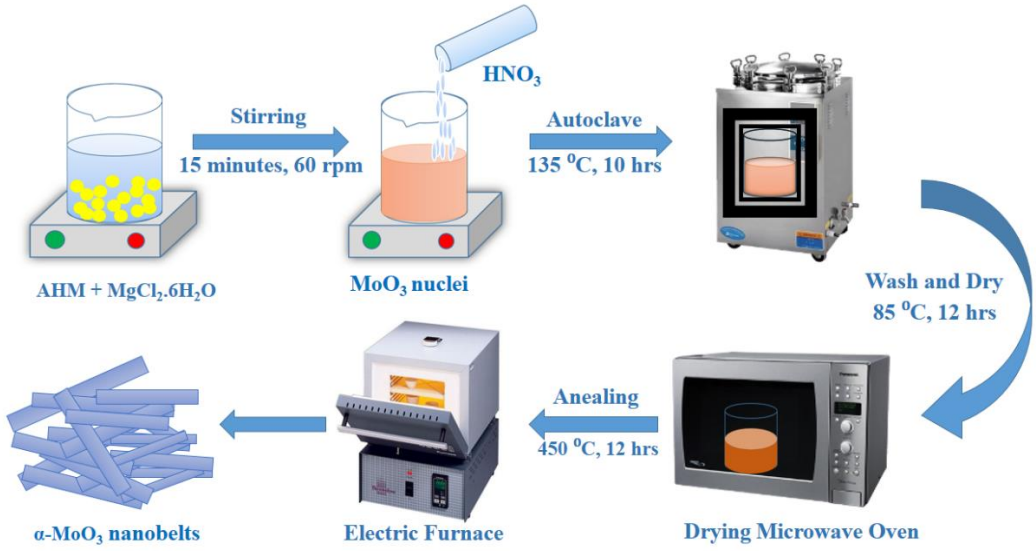

Figure 1: Schematic diagram of Mg-doped α-MoO_3 nanobelts formation.

2.2 Methods of characterization

The crystallographic arrangements and phases of both specimens were analyzed using an XRD specifically, the 3040-*X*'Pert PRO model. Scans were conducted at a rate of 1°/minute within the 10 – 60° range. The primary beam was set to 40 kV and 30 mA for generating CuKα (λ = 1.54056 Å) radiation. The surface characteristics were examined using a field emission scanning electron microscope (FESEM) with a *JEOL JSM-7600F* model. An accelerating voltage of 5 kV was employed. For exploring functional groups and the phase stability of the samples, Fourier-transform infrared spectroscopy (FTIR-ATR) was employed, utilizing a Perkin Elmer Spectrum Two model. This analysis was conducted across a wavenumber range of 4000–400 cm^{-1}. The optical attributes of the nanobelts were investigated with a UV-Vis-NIR diffuse reflectance spectrophotometer, specifically the Lambda 1050 model from PerkinElmer (USA). This examination covered wavelengths ranging from 200 to 800 nm.

3. RESULTS AND DISCUSSION

3.1 Surface Morphology Analysis

Figure 2(a - d) display the typical micrographs of Field Emission Scanning Electron Microscope (FESEM) images show casing as-synthesized pristine α-MoO_3 and Mg-doped α-MoO_3 nanobelts with 2%, 4%, and 6% Mg doping concentrations, respectively. The pristine sample's overall morphology reveals a high degree of uniformity, primarily comprised of straight and densely packed nanobelts. The SEM image shows that these nanobelts have smooth surfaces and are distributed randomly, although these nanobelts have slight adjustments in their crystallite sizes. The rapid nucleation process contributes to the haphazard arrangement of the nanobelts. Notably, each nanobelt's flat, rectangular tip exhibits sharp corners. Regarding the impact of Mg content on nanobelt evolution following its incorporation into the pristine sample, drawing definitive conclusions is challenging, and apparent alterations are not discernible.

The average length of nanobelts of pure and Mg doped α-MoO_3 varies between 1.493 to 1.784μm and average width varies between 157 to 252nm showed in Table 1. Similar nanobelt like shape are observed in our previous experiment about Fe-doped α-MoO_3[34].The expected highly crystalline samples can be checked by XRD powder diffraction experiment as described in the next coming study. Phuruangrat *et al* reported the hydrothermally synthesized W-doped MoO_3 nanobelts and our present results are in good agreement with their result [29].The nanobelts displayed widths varying between 50 and 150 nm, while their lengths were approximately 1–5nm. These nanobelts possess a sleek, flat structure with rectangular tips featuring four distinct sharp corners at their terminations.

The specimens are total composition of nanobelts with varying crystalline size is apparent length ranges from 2 to 40μm. They have identical thicknesses and widths of 500nm and 1 μm, respectively. We may anticipate that the created materials will have a high crystallinity based on the observed shape of the particles. These findings are in close agreement with the work of Ying et al. [27] who used sodium molybdate (Na_2MoO_4) and fluoboric acid (HBF4) to create orthorhombic MoO_3 (α-MoO_3) nanobelts with dimensions of 300 nm in width, 50 nm in thickness, and 2–5 m in length. Navgire et al. [28] found similar outcomes. In conclusion, it is challenging to infer the Zn-doping influence on the development of the overall dimensions associated with the Zn-nanobelts from the SEM pictures. As can be seen from the overall morphological analysis, pure *h*-MoO_3 as obtained has a homogeneous belt-like shape with an irregular distribution, with a typical width of 100–150nm and a length of 1000–1800 nm. The majority of *h*-MoO_3 nanobelts are surface-flat.

The product is primarily composed of densely packed, sleek surfaces. These surfaces are completely even, absolutely straight, and arranged in a random orientation. The nanosheets have an average width ranging from 100 to 200nm and a length of a few microns.

From FESEM images it is found the physical appearance of the surface the pure α-MoO_3 and 2, 4 and 6 M% Mg doped α-MoO_3 samples consist of uniform nanobelts. The nanobelts showcase even surfaces and level rectangular tips, each exhibiting four distinct sharp corners at their terminations. Anukorn Phuruangrat *et al.* in 2016 hydrothermally synthesized *W*-doped MoO_3 nanobelts and found the similar result with us [29]. The nanobelts are randomly distributed for both pure and Mg doped α-MoO_3. The rapid nucleation leads to the random distribution of the nanobelts. The average length of nanobelts of pure and Mg doped α-MoO_3 varies between 1.493 to 1.784μm and average width varies between 157 to 252nm showed in Table-1. These findings are in strong accord with Amal L. Al-Otaibie et al.'s work, which involved the synthesis of Zn-doped orthorhombic MoO_3 (α-MoO_3)

nanobelts with dimensions of 300 nm in width and 2–5 μm. [35]. From Figure 2 (a-d) the morphology of pure and Mg-doped α-MoO_3 nanobelts have no obvious variation. It shows that the reaction environments were perfect for the evolution of nanobelts.

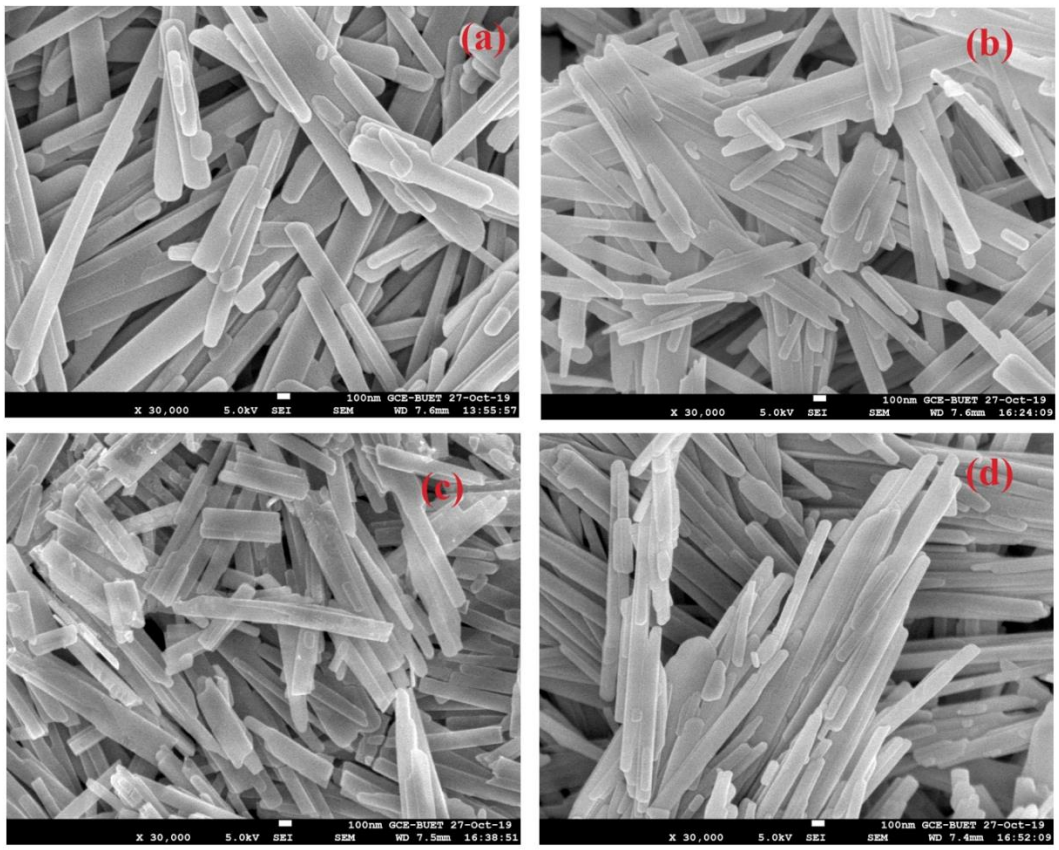

Figure 2: SEM image of pure (a) and Mg-doped 2%(b), 4%(c), 6%(d) α-MoO_3 nanobelts.

Table 1: Average length and width of pure and Mg doped α-MoO_3 nanobelts.

Mg concentration (M%)	Avg. length of nanobelts (μm)	Avg. width of nanobelts (nm)
0	1.562	252
2	1.784	235
4	1.493	181
6	1.573	157

3.2 Elemental Analysis

Energy Dispersive X-ray analysis is an approach employed to ascertain the elemental composition of a specific sample. The energy spectrum of pure and 2, 4 and 6 M% Mg doped α-MoO_3 are shown in Figure 3 (a-d). The observed peaks at 2.293 KeV and 0.525 KeV confirmed that the pure α-MoO_3 nanobelts were composed of Mo and O. The mass and atomic percentages for all samples are tabulated in Table-2 for 0, 2, 4 and 6 M% Mg doped α-MoO_3 respectively. These EDX spectra insure the presence of O, Mo and Mg in all doped samples. The observed peaks at 0.525 KeV, 2.293 KeV and 1.253 KeV indicate the presence of O, Mo and Mg respectively [31].

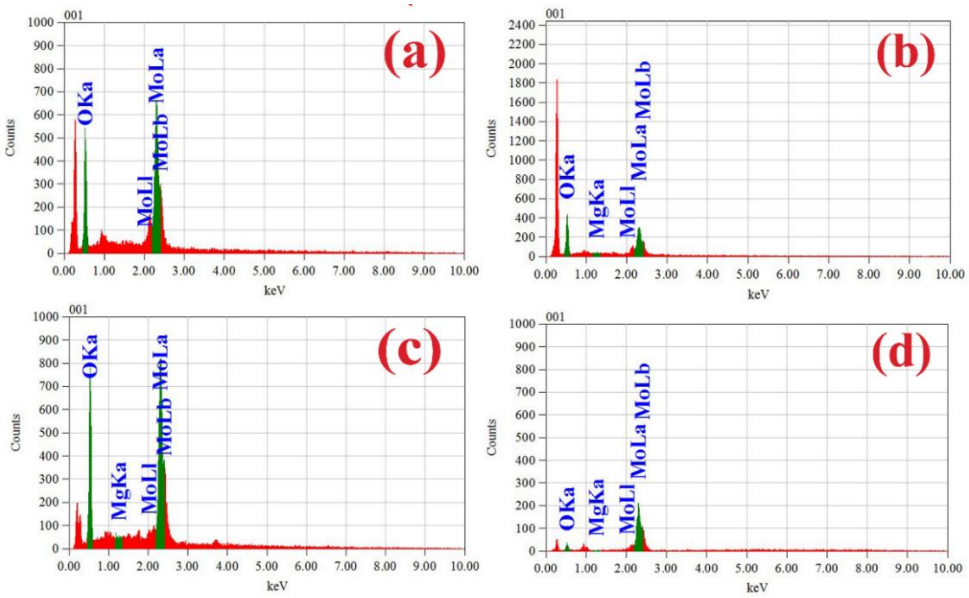

Fig. 3: EDX spectra of pure (a) and Mg-doped 2%(b), 4%(c), 6%(d) α-MoO_3 nanobelts.

Table2: The mass and atomic percentage of pure and Mg-doped α-MoO_3 nanobelts.

Mg concentration (M%)	Elements	Mass %	Atom %
0	O	41.31	79.95
	Mo	58.69	20.05
2	O	53.49	87.25
	Mg	0.13	0.14
	Mo	46.39	12.62
4	O	37.88	78.41
	Mg	0.15	0.21
	Mo	61.97	21.39
6	O	19.34	58.86
	Mg	0.14	0.29
	Mo	80.51	40.85

These results are show that Mo has the highest % of mass and oxygen has the highest % of atom within Mg doped α-MoO_3 nanobelts. From the results it is sure that mass and atomic % of O, Mo and Mg varies slightly within Mg doped α-MoO_3 nanobelts.

3.3 Structural properties

The structural properties are investigated of both undoped and Mg-doped α-MoO_3 nanobelts at different mol percentages (0, 2, 4, and 6 M% Mg) using powder XRD patterns, as shown in Figure 4. The diffraction pattern was obtained at room temperature, covering an angle range of 10º to 60º ($10^º \leq 2\theta \leq 60^º$), employing a Philips PW 3040 X' Pert PRO XRD system. The scan rate was set at 1°/min with a primary beam power of 40 kV and 30 mA for CuKα (λ = 1.54056Å) radiations. The diffraction peaks corresponding to pure α-MoO_3 nanobelts were identified at 12.71º, 23.30º, 25.67º, 27.28º, 33.69º, 35.45º, 38.96º, 46.31º, and 58.84º are aligning with the (020), (110), (040), (021), (111), (041), (060), (210), and (081) crystallographic planes (*hkl*), respectively. The observed XRD pattern confirms the polycrystalline nature of the synthesized samples, exhibiting a thermodynamically stable α orthorhombic structure for pure MoO_3[36].The diffraction peaks of the pure orthorhombic α-MoO_3 phase were matched with the experimental data, demonstrating lattice constants: a = 3.9668Å, b = 13.8680Å, and c = 3.7018Å, which align well with JCPDS card No. 05-0508 [37]. No intermediate peaks or impurities were discerned from the XRD data, indicating the proper incorporation of the Mg element into the MoO_3 crystal lattice without significantly disrupting the orthorhombic structure of α-MoO_3. Figure 5 reveals slight peak shifting attributed to the relatively close atomic radii of Mg^{2+} (0.57Å) and Mo^{6+} (0.62Å).Similar peak shifting phenomena were observed in studies by M. Kovendhan et al. [38] for Li -doped α-MoO_3 thin films, Kumar et al. [39] forTb-doped α-MoO_3 nanostructures, Illyaskutty et al. [40] for Zn-incorporated MoO_3 thin films and Bai et al.[31] for Zn-doped α-MoO_3nanobelts.The XRD pattern confirms that the prominent peaks correspond to (220) reflection intensities, representing the anisotropic growth of the nanobelts and affirming the crystal orientation along the *b*-axis of the orthorhombic structure [21].

The diffraction peaks along the (0k0) planes (where k = 2, 4, 6) exhibit a higher intensity in comparison to the standard JCPDS data, suggesting a preferential orientation. The preferred orientation positions for α-MoO_3 are found at 12.71º, 25.67º, and 38.96º. These positions slightly deviate from the positions 12.72º, 25.68º, 38.98º; 12.72º, 25.68º, 38.98º; and 12.73º, 25.70º, 38.99º for the 2, 4, and 6 M% Mg-doped α-MoO_3, respectively. This suggests minimal peak shifting, indicating negligible lattice strain and insignificant changes in inter-planar spacing [41]. As the concentration of Mg increases in α-MoO_3, the intensity of the diffraction peaks decreases. This variation in intensity demonstrates that the number of planes oriented along the (020) direction diminishes with the higher concentration of Mg in α-MoO_3[42].

The XRD acts as a valuable analytical technique for assessing the structural attributes of crystals. The examination of XRD patterns offers valuable information about the configuration of crystalline substances, including lattice constants, lattice strain, atomic arrangement, crystallite size, dislocation density, existence of stacking faults, and deviations stemming from favored orientation (040).

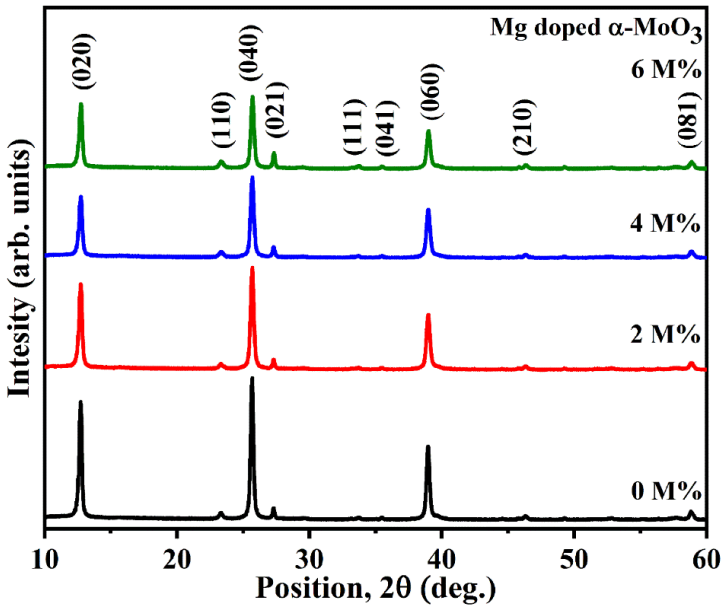

Fig. 4: XRD pattern of pure α-MoO_3 and Mg-doped α-MoO_3 nanoparticles.

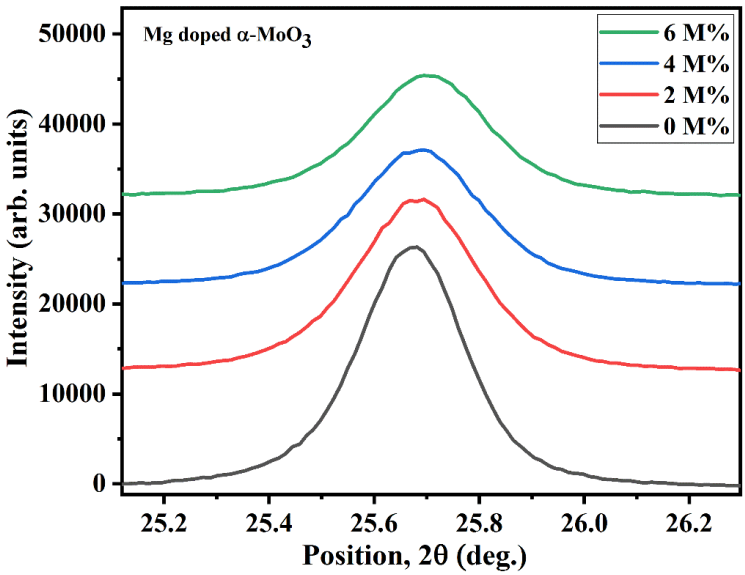

Fig. 5: XRD peak broadening of pure and Mg doped α-MoO_3 nanobelts for (040) plane.

The determination of lattice constants for the orthorhombic α-MoO_3 nanobelts can be performed using the subsequent equation: [5].

$$\frac{1}{d_{hkl}^2} = \frac{h^2}{a^2} + \frac{k^2}{b^2} + \frac{l^2}{c^2}$$

Where d_{hkl} is the inter-planar spacing of the (*hkl*) plane and *a*, *b* and *c* symbolize the lattice constants. For orthorhombic phase $a \neq b \neq c$ and $\alpha = \beta = \gamma = 90^0$. The lattice constant is measured for the (*hkl*) plane and the lattice constants are *a* = 3.96 Å, *b* = 13.86 Å and *c* = 3.70 Å shown in Table 3.

The change in peak intensity corresponds directly related to crystallinity, while the alteration in the full width at half maximum (FWHM) is linked to the size of the crystallites.The average crystallite size (D_v) can be obtained using the well-known Debye–Scherrer's formula [5].

$$D_v = \frac{k\lambda}{\beta_{hkl}\cos\theta_{hkl}}$$

In this context, D_v represents the average crystallite size computed by volume weighting. The symbol λ corresponds to the wavelength of X-ray radiation (λ = 1.54056 Å for CuKα). The term *K* signifies the shape factor, set at *K* = 0.90. β_{hkl} stands for the corrected FWHM of the diffraction peak, measured in radians, and situated at the 2θ Bragg's angle, expressed in degrees.

3.4 Stacking Fault

Stacking faults are structural characteristics that elucidate crystal imperfections through the analysis of powder XRD patterns. When a stacking fault exists, it can manifest as a shift in the position of the XRD reflection peak or an increase in peak width [43]. Stacking faults are regarded as planar defects. The subsequent equation is employed to calculate stacking fault (SF) values:

$$SF = \left[\frac{2\pi^2}{45(3\tan\theta_{hkl})^{\frac{1}{2}}}\right]\beta_{hkl}$$

The stacking fault values of pristine and magnesium-doped α-MoO_3 are provided in Table 3. In the case of pure α-MoO_3, the average stacking fault value is 0.00233. Upon introducing 2% Mg doping in α-MoO_3 nanobelts, this value increases to 0.00494. However, as the Mg doping concentration is further increased to 4% and 6%, the stacking fault value gradually decreases, resulting in values of 0.00305 and 0.002716, respectively, for the 4% and 6% Mg-doped samples. The stacking fault values are veries in the range from 0.002781 to 0.00494.

Table 3: Variation of peak position, FWHM, inter-planer distance, stacking fault, lattice parameters and unit cell volume.

Sample M%	Miller Indices (*hkl*)	Position, $2\theta_{hkl}$ Deg.	FWHM Deg.	Inter-planer distance nm	Stacking fault	Lattice parameters (Å)			Unit cell volume $(Å)^3$
						a	*b*	*c*	
0	(020)	12.7156	0.2378	0.6956	0.0031	3.9668	13.8680	3.7018	203.6435
	(110)	23.3048	0.3079	0.3813	0.0030				
	(040)	25.6706	0.2373	0.3467	0.0022				
	(021)	27.2875	0.1889	0.3265	0.0016				
	(111)	33.6999	0.3281	0.2657	0.0026				
	(041)	35.4582	0.1451	0.2529	0.0011				
	(060)	38.9665	0.2638	0.2309	0.0019				
	(210)	46.3175	0.3985	0.1958	0.0026				
	(081)	58.8462	0.4404	0.1568	0.0025				
2	(020)	12.7185	0.2725	0.6954	0.0108	3.9641	13.8640	3.7009	203.4010
	(110)	23.3198	0.3489	0.3811	0.0074				
	(040)	25.6808	0.2889	0.3466	0.0056				
	(021)	27.2945	0.1907	0.3264	0.0034				
	(111)	33.6893	0.2258	0.2658	0.0033				
	(041)	35.4611	0.2415	0.2529	0.0033				
	(060)	38.9759	0.3082	0.2309	0.0038				
	(210)	46.3248	0.3043	0.1958	0.0031				
	(081)	58.8562	0.4440	0.1567	0.0034				
	(020)	12.7203	0.2885	0.6953	0.0016	3.9624	13.8680	3.7006	203.3526
	(110)	23.3288	0.4313	0.3810	0.0034				
	(040)	25.6838	0.2793	0.3465	0.0023				
	(021)	27.2943	0.2172	0.3264	0.0018				

Sample M%	Miller Indices (*hkl*)	Position, $2\theta_{hkl}$ Deg.	FWHM Deg.	Inter-planer distance nm	Stacking fault	Lattice parameters (Å)			Unit cell volume $(Å)^3$
						a	*b*	*c*	
	(111)	33.6743	0.4114	0.2659	0.0039				
4	(041)	35.4828	0.1373	0.2527	0.0013				
	(060)	38.9796	0.3117	0.2308	0.0032				
	(210)	46.3236	0.3397	0.1958	0.0039				
	(081)	58.8588	0.4261	0.1567	0.0056				
	(020)	12.7311	0.2906	0.6947	0.00385				
	(110)	23.3451	0.4407	0.3807	0.00429				
	(040)	25.7004	0.2809	0.3463	0.0026				
	(021)	27.3154	0.2205	0.3262	0.00198				
	(111)	33.7028	0.3431	0.2657	0.00276	3.9597	13.8540	3.698	202.8637
6	(041)	35.4864	0.3532	0.2527	0.00276				
	(060)	38.9987	0.3205	0.2307	0.00238				
	(210)	46.4321	0.2607	0.1954	0.00176				
	(081)	58.8748	0.4506	0.1567	0.00265				

3.5 Williamson-Hall Analysis

The Scherrer formula allows us to determine the crystallite size based on line broadening. However, certain other microstructural characteristics such as intrinsic strain, which emerges within nanocrystals due to factors like point defects, grain boundaries, and stacking faults, remain undisclosed through this formula.[44]. The Williamson-Hall method addresses these limitations through X-ray line broadening analysis [17], employing various models such as the uniform deformation model, uniform deformation stress model, and uniform deformation energy density model[45].

The Williamson–Hall analysis simplifies the integral breadth method, proposing that the broadening of X-ray diffraction peaks is a result of both the size and micro-strain within the nanocrystals. The total broadening can be expressed as:

$$\beta_{hkl} = \beta_s + \beta_D$$

β_{hkl} signifies the FWHM of a peak in radians, while β_s and β_D stand for the contributions to the peak broadening attributed to size and strain, respectively. In the Williamson-Hall relationship, uniform strain across all crystallographic directions is assumed, resulting in the following expression for β_{hkl}:

$$\beta_{hkl} = \frac{k\lambda}{D\cos\theta} + 4\varepsilon \tan\theta$$

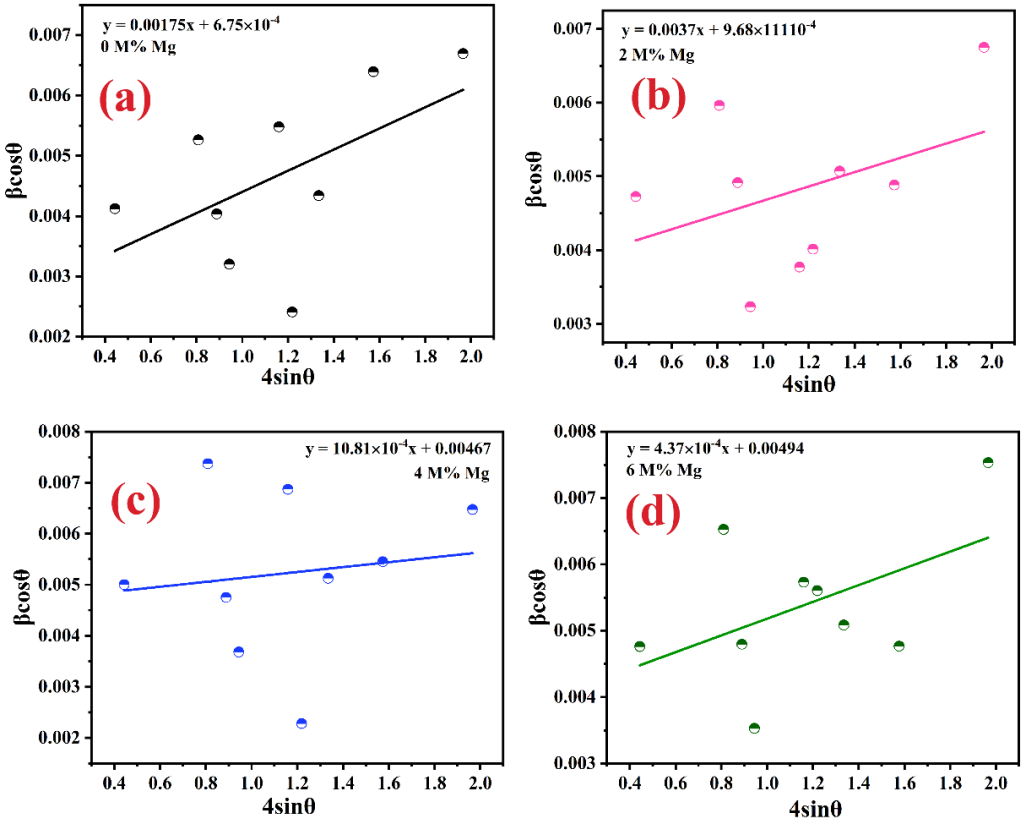

Fig. 6: The W-H plot of (a) pure α- MoO_3 (b) 2 M% (c) 4 M% and (d) 6 M% Mg-doped α-MoO_3 nanobelts.

Rearranging the equation, we get

$$\beta_{hkl}\cos\theta = \frac{k\lambda}{D} + 4\varepsilon \sin\theta$$

The mentioned linear equations are Williamson-Hall (W-H) equations, where *D* represents the value of crystallite size, and ε stands for micro-strain. A graph is constructed using $4sin\theta$ on the *x*-axis and $\beta_{hkl}cos\theta$ on the *y*-axis for the nanoparticles that were prepared, as illustrated in Figure 6. By performing a linear regression analysis on the data, the crystalline size is determined from the *y*-intercept, while the strain ε is derived from the slope of the fit.

3.6 Halder-Wagner analysis

In the realm of solid-state physics (SSP), it's recognized that the XRD peak profile is approximated by the Lorentzian function, whereas the strain broadening follows a Gaussian function. It is well-known to us that the XRD peak doesn't precisely adhere to either the Lorentzian or Gaussian function. This situation leads us to categorize the XRD peak into two parts: the central peak region, which aligns more closely with the Gaussian function, and the trailing tail region, which corresponds better to the Lorentzian function [46][47]. Halder and Wagner introduced a solution to this challenge by introducing a symmetric Voigt function, which results from the convolution of the Lorentzian and Gaussian functions [47][48]. Consequently, when employing the Voigt function, the FWHM in the Halder-Wagner method can be expressed as:

$$\beta_{hkl}^2 = \beta_l \beta_{hkl} + \beta_G^2$$

where β_l and β_G are the FWHM of Lorentzian and Gaussian function.

It should be mentioned that Halder-Wagner (HW) has another idea about the determination of *D* and ε from XRD data [36].They suggested a different formula that included the reciprocal lattice point's integral breadth, β*, and the reciprocal cell's lattice plane spacing, *d**.

$$\left(\frac{\beta^*_{hkl}}{d^*_{hkl}}\right)^2 = \frac{1}{D_{HW}}\frac{k\beta^*_{hkl}}{{d^*_{hkl}}^2} + (2\varepsilon_{HW})^2$$

Where D_{HW} and $\varepsilon_{HW}$are Halder–Wagner crystallite size and strain, respectively and β*and *d**can be expressed as follows:

$$\beta^* = \frac{\beta\cos\theta}{\lambda}$$

$$d^* = \frac{2\sin\theta}{\lambda}$$

On the assumptions that the Lorentzian and Gaussian components of β* are solely due to the size and strain effects, respectively. Putting the values of β* and

$$\left(\frac{\beta}{\tan\theta}\right)^2 = \frac{K\lambda}{D_{HW}}.\frac{\beta}{\tan\theta\sin\theta} + 16{\varepsilon_{HW}}^2$$

Rearranging the above equation

$$\left(\frac{\beta\cos\theta}{\sin\theta}\right)^2 = \frac{K\lambda}{D_{HW}}.\frac{\beta\cos\theta}{\sin^2\theta} + 16{\varepsilon_{HW}}^2$$

$$\text{or,} \quad \left(\frac{\beta}{\tan\theta}\right)^2 = \frac{K\lambda}{D_{HW}}.\frac{\beta}{\tan\theta\sin\theta} + 16{\varepsilon_{HW}}^2$$

In the H-W technique, a plot of $\left(\frac{\beta}{\tan\theta}\right)^2$ is made against $\frac{\beta}{(\tan\theta\sin\theta)}$ which shows a straight line of slope$\frac{K\lambda}{D_{HW}}$and intercept$16\varepsilon_{HW}{}^2$. The Figure 7 represent the Halder–Wagner crystallite size (D_{HW}) and the intercept provides the Halder–Wagner strain (ε_{HW}).

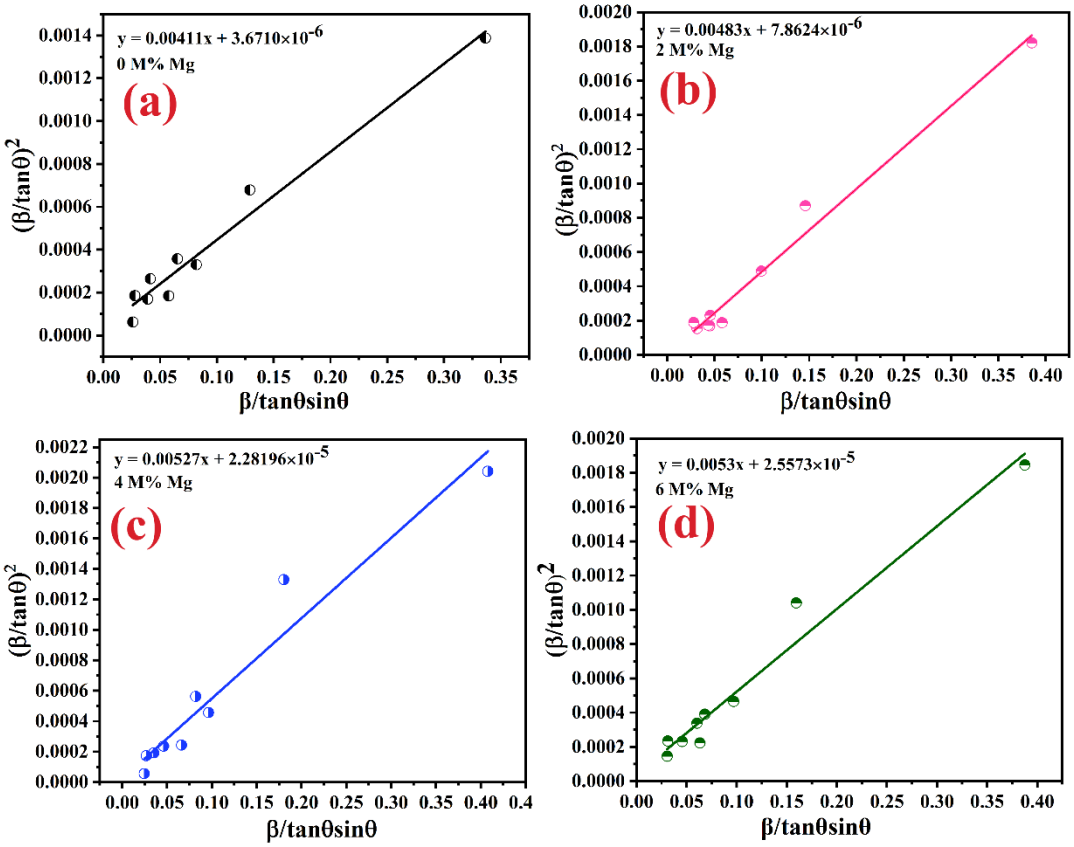

Fig. 7: The H-W plot of (a) pure α- MoO_3 (b) 2 M% (c) 4 M% and (d) 6 M% Mg-doped α-MoO_3 nanobelts.

3.7 Dislocation Density (δ)

Dislocation defects, also referred to as topological defects, serve as indicators of crystallographic imperfections within a crystalline substance. The mobility of dislocations is hindered by the presence of other dislocations within the material. Consequently, an elevated dislocation density implies greater hardness. The dislocation density (δ) can be calculated using the subsequent equation [49].

$$\delta = \frac{1}{D_v^2}$$

Here, δ represents the dislocation density, and D_v indicates the volume-weighted average crystallite size in nm. The mean dislocation density of both unmodified and magnesium-doped α-MoO_3 nanobelts was determined using the D-S, W-H and H-W teqniques, as detailed in Table 4. The dislocation density values calculated through the D-S method are higher compared to those from the W-H method. This disparity arises because dislocation density is reciprocal to the square of crystalline size, and smaller crystalline sizes are observed with the Debye Scherrer method. So it's evident that the dislocation density increases with increasing doping concentration.

3.8 Stokes-Wilson (S-W) Methods

Lattice strain contributes to the broadening of XRD lines, a phenomenon arising from the emergence of crystal defects like imperfections and distortions [50]. The deviations of atoms from their reference-lattice positions within the crystal are accountable for the development of these defects [51]. The mean lattice strain (ε) can be evaluated using the S–W equation given below[52].

$$\varepsilon = \frac{\beta_{hkl}}{4\tan\theta_{hkl}}$$

The r.m.s values of microstrain (ε_{rms}) along the different crystallographic planes can be determined by using S-W relation

$$\varepsilon_{rms} = \sqrt{\frac{2}{\pi}}\varepsilon$$

Figure 8 correspondentsε_{rms} versus ε plot. The data should form a linear arrangement along a 45-degree angle relative to the horizontal axis. The root mean square strain changes uniformly in relation to micro-strain, suggesting the absence of any inconsistencies linked to the crystallographic orientation of lattice planes.

The results are obtained for crystalline size and strain using D-S, W-H, and H-W techniques show substantial differences, as illustrated in Table-4. According to the D-S formula, the average crystalline size is measured at 32.74 nm for pure MoO_3, whereas it registers as 52.32 nm and 33.82 nm when evaluated using the W-H and H-W approaches, respectively. Notably, the value of D derived from the W-H method markedly surpasses the values yielded by the D-S and H-W techniques. The mean crystallite size and lattice strain values determined through the D-S, W-H and H-W methods consistently exhibit a comparable trend, as summarized in Table 3 for all samples. Upon introducing Mg into the MoO_3 compound, the average crystallite size experiences a reduction, indicating a reduction in crystallinity due to the replacement of Mo with Mg within the MoO_3 lattice structure [36]. This drop in average crystalline size can be attributed to the defects are resulting from Mg doping in pure α-MoO_3. Such a phenomenon can be linked to the difference in ionic radii between Mg^{+2} (0.57 Å) and Mo^{6+} (0.65 Å) [36], which impedes the crystal formation and growth of α-MoO_3.

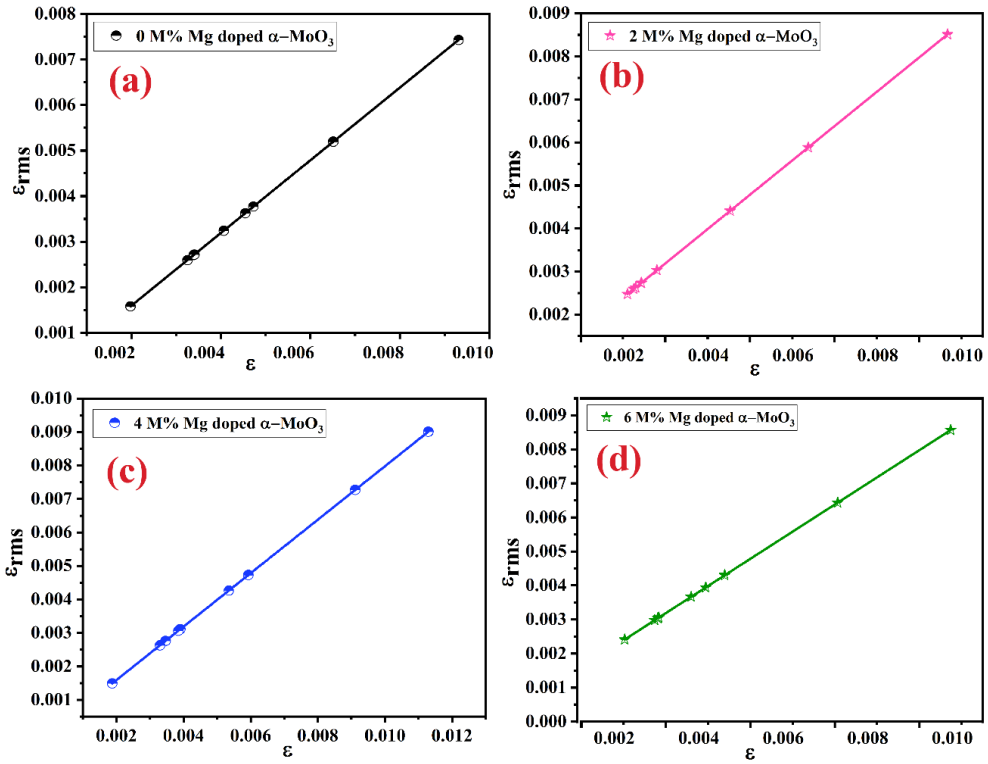

Fig. 8: ε_{rms} versus ε graph of (a) pure α- MoO_3 (b) 2 M% (c) 4 M% and (d) 6 M% Mg-doped α-MoO_3 nanobelts.

Table 4: Data for various structural parameters of MoO_3 samples obtained from Scherrer, W-H and H-W methods.

Sample (M %)	S-W method		D-S method		W-H method			H-W method		
	ε 10^{-3}	ε_{rms} 10^{-3}	D Nm	δ lines/nm^2 10^{-4}	D_{W-H} nm	ε_{W-H} 10^{-4}	δ lines/nm^2 10^{-4}	D_{H-W}	ε_{H-W} 10^{-4}	δ lines/nm^2 `10^{-4}
0	4.577	3.65	32.74	9.320	52.32	6.75	3.65	33.82	4.79	8.74
2	4.877	3.89	30.14	11.00	37.47	9.686	7.12	28.71	7.010	12.14
4	5.340	4.26	29.79	11.26	29.69	10.81	11.34	26.31	11.94	14.44
6	5.539	4.41	26.91	13.80	28.07	13.71	12.69	26.16	15.87	14.61

3.9 Fourier Transform Infrared (FTIR) Spectroscopy Analysis

FTIR was employed to capture the infrared absorption, emission, and photoconductivity spectra across solid, liquid, and gaseous phases, within a specified wave number range. FTIR was also utilized to identify impurities and ascertain the chemical bonding interactions between molybdenum and oxygen atoms within MoO_3, as well as any other bonding formations within synthesized crystal structure. In this study, FTIR was utilized to record the distinct functional groups present in both pristine and Mg-doped α-MoO_3 nanobelts, covering a wave number range of 4000 to 400 cm^{-1} within the mid-IR region wavelength. These results are depicted in Figure 9.

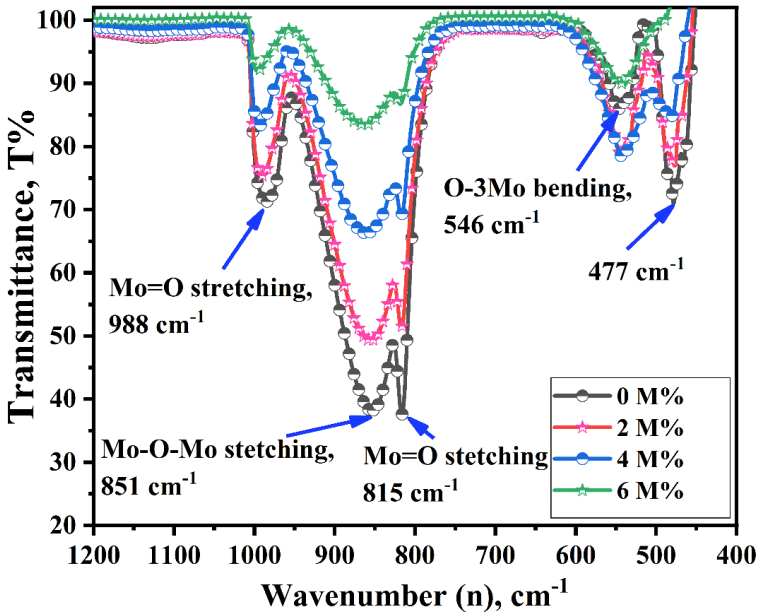

Figure 9: FTIR spectra of pure α- MoO_3 and 2, 4, 6 M% Mg-doped α-MoO_3 nanobelts.

The primary vibrational regions for α-MoO_3 oxide are 1000–600 cm^{-1} and 600–400 cm^{-1}. In the case of pure α-MoO_3 oxide, four robust vibration peaks were identified within the 1000–600 cm^{-1} range, specifically at 988, 851, 815, and 546 cm^{-1}. Upon introducing Mg doping, distinct characteristic peaks were observed: 990, 855, 816, and 547 cm^{-1} for 2M% Mg-doped α-MoO_3 nanobelts; 992, 860, 816, and 547 cm^{-1} for 4M% Mg-doped α-MoO_3 nanobelts; and 996, 863, 817, and 548 cm^{-1} for 6M% Mg-doped α-MoO_3 nanobelts. These findings are detailed in Table 5. In the 600–400 cm^{-1} range, there is a faint vibration at 477 cm^{-1} for pure α-MoO_3 and vibrations at 479, 481, and 489 cm^{-1} for 2, 4, and 6 M% Mg-doped α-MoO_3, respectively. The faint peak observed at 467 cm^{-1} originates from the bending mode of the Mo–O–Mo unit [53], and the strength of this band diminishes as the Mg concentration rises. The FTIR spectrum displays two prominent characteristic peaks at 815 and 988 cm^{-1}, associated with the terminal Mo=O stretching vibration. This signifies the presence of the layered orthorhombic MoO_3 phase, further corroborating the findings from XRD analysis [35][54].The absorption peak at 851 cm^{-1} is attributed to the stretching mode of oxygen in Mo–O–Mo bonds. This recurrence indicates that the bond lengths along the two

sides of O in Mo–O–Mo are symmetrical, which results from the shared corner oxygen between the two MoO_6 octahedra [54]. The following broad peak at 546 cm^{-1} is associated with the flexing motion of an oxygen atom attached to three metal atoms[55]. There was no indication of water presence in this product with an orthorhombic structure. A subtle deformation is observed at 550 cm^{-1} in the MoO_3 structure, with a similar broadening being noted in other studies on Zn-doped α-MoO_3 nanobelts [35] , as well as Ni and Co-doped α-MoO_3 nano powders [56]. The impact of the dopant can introduce minor imperfections in the materials, thereby fostering increased short-range disorder.

Table 5: Functional group analysis for pure α-MoO_3 and 2, 4, 6 M% Mg-doped α-MoO_3 nanobelts.

Functional group	**Wavenumber, n (cm^{-1})**			
	0 M%	2 M%	4 M%	6 M%
Mo=O stretching	988	990	992	996
Mo-O-Mo stretching	851	855	860	863
Mo=O stretching	815	816	816	817
O-3Mo bending	546	547	547	548
O-Mo-O bending	477	479	481	489

3.10 Optical properties and band gap energy

The optical properties of α-MoO_3 nanoparticles with varying concentrations of Mg (2%, 4%, and 6%) were investigated using diffuse reflection UV–vis absorbance spectroscopy, a standard technique for assessing the optical characteristics of powdered nanomaterials[57]. Figure 10 presents the UV-vis-NIR diffuse reflectance spectroscopy (DRS) data for both pure and Mg-doped samples, with reflectance measurements taken within the range of 200 to 800 nm. The figure illustrates that in the ultraviolet region, both undoped and doped samples exhibit very low reflectance. As the region shifts towards the intermediate range, the reflectance increases steeply. Within the visible range (400 to 690 nm), a notable increase in reflectance is observed. Moreover, the reflectance value decreases with the rising concentration of Mg in α-MoO_3. This phenomenon is attributed to the band gap transition of MoO_3, specifically the transition from the conduction band (Mo- 4*d*) to the valence band (O-2*p*) [58].

Distinct reflectance spectra are observed at approximately 476 nm, prompting the calculation of the optical band gap using the Kubelka–Munk (K–M) function for various wavelengths[35].

$$\frac{K}{S} = \frac{(1 - R_\infty)^2}{2R_\infty} = F(R_\infty)$$

Where *S*represents the scattering coefficient and K represents absorption coefficient, and $R\infty$ represent the diffuse reflectance. R_∞ is termed the Kubelka-Munk function, which is proportional to

the absorption coefficient α. Within a parabolic band arrangement, the connection between the bandgap and absorption coefficient is established by the widely recognized Tauc correlation[59]:

$$F(R)_\infty = \alpha = \frac{(h\nu - E_g)^n}{h\nu}$$

or

$$(\alpha h\nu)^{1/n} = A(h\nu - E_g)$$

where E_g corresponds to the band gap energy, α represent the absorption coefficient where $h\nu$ represents the photon's energy of the sample. A is a constant subject to the electron transition from the valence band to the conduction band and the transition parameter, n represents 2, 1/2, 3 or 3/2 for indirect allowed, direct allowed, indirect forbidden and direct forbidden transitions respectively. It is well known that MoO_3 represent the direct transition family so n will take the value ½ and the previous equation takes the form

$$(\alpha h\nu)^2 = A(h\nu - E_g)$$

Creating a graph of the squared value of ($\alpha h\nu$) against $h\nu$ and extending the linear segment to the horizontal axis results in data points, the bandgap energy of pristine and doped nanobelts. The assessed bandgap energy (E_g)using K-M function are 3.05, 3.10, 3.12 and 3.15 eV for 0, 2, 4 and 6 M% Mg-doped α-MoO_3nanobelts, respectively as shown in Figure 11.Our findings of band gap values for pristine and doped orthorhombic molybdenum trioxide are too close to the range of reported values by Cheng et al. [37] for nanoribbons (3.18 eV) and Scirè *et al.*[60]for thin film (3.26 eV). The increasing trend of band energy within range 2.05-2.15eV and with Mg doping concentration indicates is the noticeable blue shift due to reasons of impurity effect, defect formation, Burstein–Moss (BM) effect [61][62], and quantum size effect [63].The similar blue shifting results also observed by Al-otaibi et al.[35] for Zn-doped α-MoO_3 nanobelts and Liu et al. [64] for Al doped layered α-MoO_3nanocrystals. From the XRD result it is clear that the crystallite size values is increased while the lattice strain and dislocation density are increased with increasing Mg concentration and implies that the crystal defects and disorder are increased gradually. Anderson's model stated that disorder is inaugurated in the crystal structure, delocalized states slowly switch to localized states. How much localization is occurred in the crystal is quantified by comparing the disorderness and the size broadening of the band energy broadening[65][66]. The absorption peak of the pristine α-$MoO_3$is at 353 nm, and from figure 10 it is at around 315 nm, inference a blue shift relative to the pristine material[67]. This blue shift is due to quantum size effect whenever a nanomaterials absorbs enough energy; it generates an electron–hole pair by exciting the charges, which cause drastic change in the optical properties [68]. The band gap is usually best explained by the Burstein–Moss (BM) effect, which is that as the carrier concentration increases after Mg doping, the Fermi level shifts to conduction band which leads to band gap energy broadening [69]. Due to the band gap widening of α-MoO_3, this materials are potentially integrated various optical sensors[70] e, g, UV-vis photodetector [71].

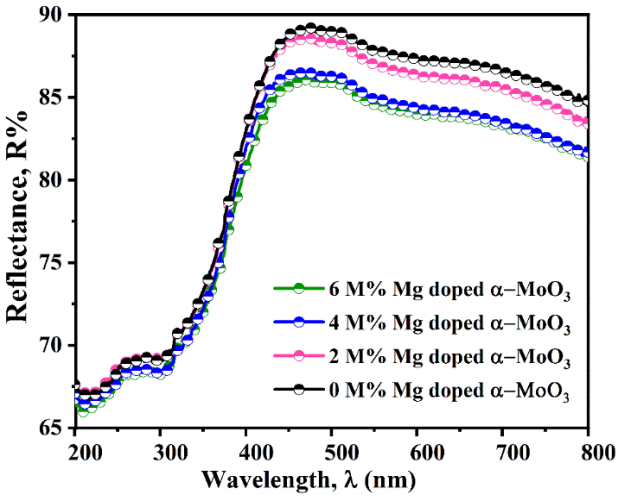

Fig. 10: Diffused reflectance spectra of as-synthesized α-MoO_3 and Mg doped α-MoO_3

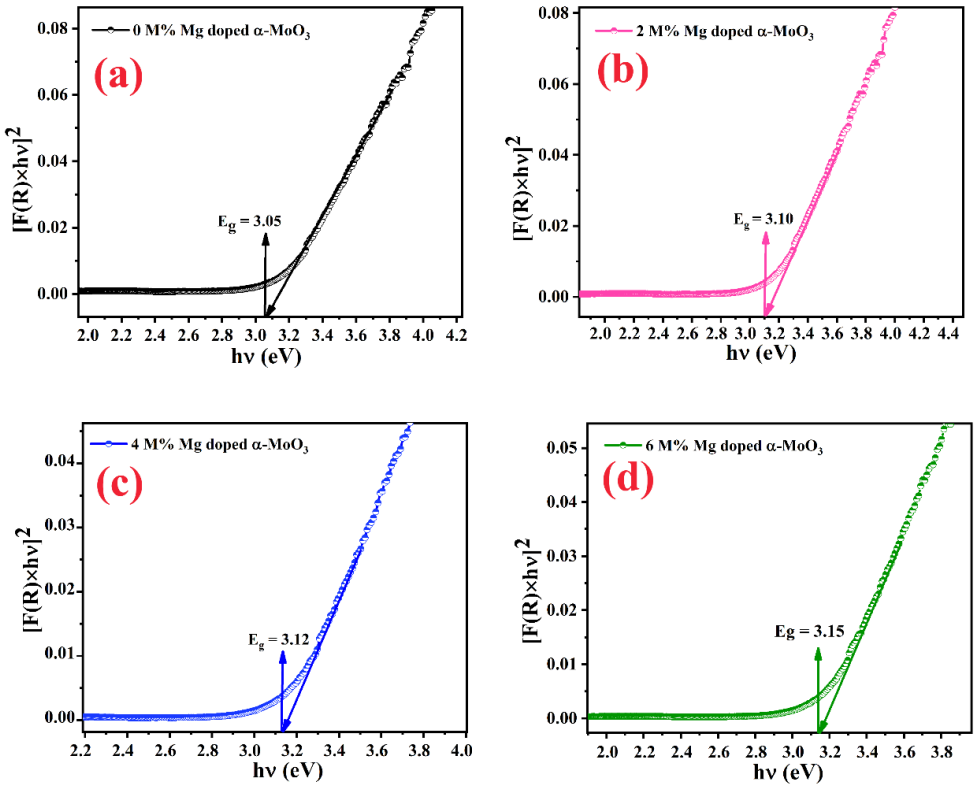

Fig. 11: Optical bandgap (E_g) of as-synthesized α-MoO_3 and different Mg doped α-MoO_3.

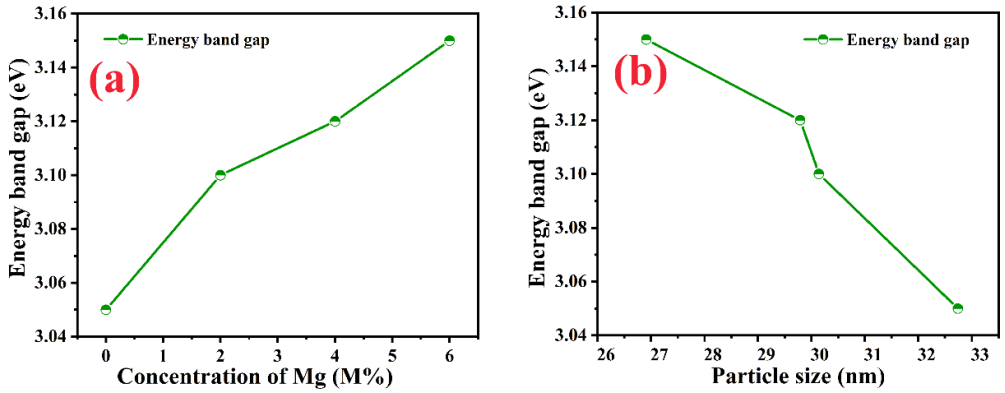

Fig. 12: Bandgap energy vs (a) doping concentration and (b) particle size for pure and 2, 4, 6 M% Mg-doped α-MoO_3 nanobelts.

4. CONCLUSIONS

The primary focus of this research is to analyze alterations in the structural, morphological, and optical attributes of α-MoO_3 nanobelts that have been doped with Mg. These nanobelts were generated using a hydrothermal methodology. The XRD results revealed the formation of an orthorhombic phase which is thermodynamically stable within the synthesized samples. There were no distinct peaks observed for MgO or Mg, indicating the successful integration of the Mg element into the crystal structure of MoO_3. This integration occurred without causing significant disturbance to the orthorhombic arrangement of the α-MoO_3 lattice, resulting in the development of a stable solid solution involving $Mo_{1-x}Mg_xO_3$ substitutions. Following the incorporation of Mg into the MoO_3 framework, there was a subtle reduction in the average crystallite size. This alteration led to a reduction in overall crystallinity, attributed to the replacement of Mo atoms by Mg atoms within the MoO_3 lattice structure. The drop in the average crystallite size is linked to the introduction of imperfections within the pure α-MoO_3 structure. Various parameters, such as FWHM, inter-planar spacing, unit cell volume, dislocation density, stacking fault, and strain, are changed their property by incorporating Mg content in α-MoO_3. To validate the orthorhombic structure of MoO_3, FTIR spectra were recorded within the wavenumber range of 4000-400 cm^{-1}. No indication of water presence was identified in this orthorhombic-configured sample. Through UV-vis spectroscopy analysis, the optical band gap (E_g) within range from 3.05 to 3.15 eV. An increasing in the band gap energy was observed as the doping percentage increased. The energy gap variations in the synthesized samples can be affected by factors such as shape, size distribution, phase, crystallinity, and imperfections. Examination of FESEM images disclosed the arbitrary dispersion of nanobelts in both pristine and Mg-doped α-MoO_3. The random distribution could be attributed to rapid nucleation. The average length of nanobelts in pure and Mg-doped α-MoO_3 ranged from 1.493 to 1.784 μm, with the average width fluctuating between 157 and 252 nm. The presence of O, Mo, and Mg in all doped samples was confirmed through the EDX spectra.

CREDIT AUTHOR STATEMENT

K. Hoque: Conceptualization, Writing - Original Draft & Supervision. **Sapan Kumar Sen**: Conceptualization, Validation, Data Curation. **Pritish Mondal**: Formal analysis &Investigation. **M. S. Manir**: Validation, Data Curation. **Supria Dutta**: Formal analysis, **Parimal Bala**: Writing - Review & Editing.

CONFLICT OF INTEREST

There is no conflict of interests present.

ACKNOWLEDGEMENT

We express our gratitude to the Physics Discipline at Khulna University for their valuable administrative support, and also extend our thanks to the Glass and Ceramic Engineering Departments at Bangladesh University of Engineering and Technology (BUET) in Dhaka, Bangladesh. Additionally, we appreciate the contributions of the Atomic Energy Research Establishment (AERE) and the Institute of Electronics under the Bangladesh Atomic Energy Commission.

REFERENCES

[1] A. Orendorz, A. Brodyanski, J. Lösch, L. H. Bai, Z. H. Chen, Y. K. Le, C. Ziegler, and H. Gnaser, *Surf. Sci.* 601, 4390 (2007).
[2] S. H. Lee, R. Deshpande, P. A. Parilla, K. M. Jones, B. To, A. H. Mahan, and A. C. Dillon, *Adv. Mater.* 18, 763 (2006).
[3] A. Khorsand Zak, W. H. Abd. Majid, M. E. Abrishami, and R. Yousefi, *Solid State Sci.* 13, 251 (2011).
[4] J. Park, E. Kang, S. U. Son, H. M. Park, M. K. Lee, J. Kim, K. W. Kim, H. J. Noh, J. H. Park, C. J. Bae, J. G. Park, and T. Hyeon, *Adv. Mater.* 17, 429 (2005).
[5] A. M. Badr, H. A. Elshaikh, and H. H. Afify
[6] A. Chithambararaj, N. Rajeswari Yogamalar, and A. C. Bose, *Cryst. Growth Des.* 16, 1984 (2016).
[7] A. Phuruangrat, S. Thipkonglas, T. Thongtem, and S. Thongtem, *Mater. Lett.* 195, 37 (2017).
[8] N. Desai, V. Kondalkar, R. Mane, C. Hong, and P. Bhosale, 1 (2016).doi:10.4172/2157-7439.1000338
[9] S. Anandan, A. Vinu, K. L. P. S. Lovely, N. Gokulakrishnan, P. Srinivasu, T. Mori, V. Murugesan, V. Sivamurugan, and K. Ariga, 266, 149 (2007).
[10] N. Moo, *Mater. Lett.* (2015).doi:10.1016/j.matlet.2015.08.031
[11] V. M. Mohan, W. Chen, and K. Murakami, *Mater. Res. Bull.* 48, 603 (2013).
[12] L. Cattin, M. Morsli, F. Dahou, S. Y. Abe, A. Khelil, and J. C. Bernède, *Thin Solid Films* 518, 4560 (2010).
[13] M. Ranjba, F. Delalat, and H. Salamati, *Appl. Surf. Sci.* 396, 1752 (2017).
[14] G. R. Mutta, S. R. Popuri, J. I. B. Wilson, and N. S. Bennett, *Solid State Sci.* (2016).doi:10.1016/j.solidstatesciences.2016.08.016
[15] D. Barreca, G. A. Rizzi, and E. Tondello, *Thin Solid Films* 333, 35 (1998).
[16] A. Kalita and M. P. C. Kalita, *Phys. E Low-dimensional Syst. Nanostructures* 92, 36 (2017).
[17] S. Anand, A. P. Amaliya, M. A. Janifer, and S. Pauline, *Mod. Electron. Mater.* 3, 168 (2017).
[18] K. Galatsis, Y. X. Li, W. Wlodarski, and K. Kalantar-zadeh, 77, 478 (2001).
[19] A. Sudha, T. K. Maity, and S. L. Sharma, *Mater. Lett.* (2015).doi:10.1016/j.matlet.2015.11.003
[20] X. Yang, H. Ding, D. Zhang, X. Yan, C. Lu, and J. Qin, 1201, 1195 (2011).
[21] A. Chithambararaj and A. C. Bose, *J. Alloys Compd.* 509, 8105 (2011).
[22] Y. Chen, C. Lu, L. Xu, Y. Ma, W. Hou, and J.-J. Zhu, *CrystEngComm* 12, 3740 (2010).
[23] A. Boukhachem, M. Mokhtari, N. Benameur, A. Ziouche, M. Martínez, P. Petkova, M. Ghamnia, A.

Cobo, M. Zergoug, and M. Amlouk, *Sensors Actuators, A Phys.* (2016).doi:10.1016/j.sna.2016.11.032
[24] W. Jiang, L. Meng, S. Zhang, X. Chuai, Z. Zhou, C. Hu, P. Sun, F. Liu, X. Yan, and G. Lu, *Sensors Actuators B. Chem.* 126888 (2019).doi:10.1016/j.snb.2019.126888
[25] S. S. Mahajan, S. H. Mujawar, P. S. Shinde, A. I. Inamdar, and P. S. Patil, *Sol. Energy Mater. Sol. Cells* 93, 183 (2009).
[26] S. Yang, Y. Liu, T. Chen, W. Jin, T. Yang, M. Cao, S. Liu, J. Zhou, G. S. Zakharova, and W. Chen, *Appl. Surf. Sci.* 393, 377 (2017).
[27] M. Vila, C. Dìaz-Guerra, D. Jerez, K. Lorenz, J. Piqueras, and E. Alves, *J. Phys. D. Appl. Phys.* 47 (2014).
[28] A. Phuruangrat, U. Cheed-Im, T. Thongtem, and S. Thongtem, *Mater. Lett.* 172, 166 (2016).
[29] A. Phuruangrat, S. Thongtem, and T. Thongtem, *Res. Chem. Intermed.* 42, 7487 (2016).
[30] Z. Li, W. Wang, Z. Zhao, X. Liu, and P. Song, *RSC Adv.* 7, 28366 (2017).
[31] S. Bai, C. Chen, D. Zhang, R. Luo, D. Li, A. Chen, and C. C. Liu, *Sensors Actuators, B Chem.* 204, 754 (2014).
[32] N. Bate, H. Shi, L. Chen, J. Wang, S. Xu, W. Chen, J. Li, and E. Wang, *Chem. - An Asian J.* 12, 2597 (2017).
[33] S. Kumar, S. Tapash, C. Paul, M. S. M. Supria, D. M. N. Hossain, and J. Podder, *J. Mater. Sci. Mater. Electron.* (2019).doi:10.1007/s10854-019-01805-z
[34] S. K. Sen, T. Chandra, M. S. Manir, S. Dutta, M. N. Hossain, and J. Podder, *J. Mater. Sci. Mater. Electron.* 30, 14355 (2019).
[35] A. L. Al-Otaibi, T. Ghrib, M. Alqahtani, M. A. Alharbi, R. Hamdi, and I. Massoudi, *Chem. Phys.* 525, 110410 (2019).
[36] S. K. Sen, S. Dutta, R. Khan, M. S. Manir, S. Dutta, and A. Al Mortuza, (2019).
[37] L. Cheng, M. Shao, X. Wang, and H. Hu, *Chem. - A Eur. J.* 15, 2310 (2009).
[38] M. Kovendhan, D. P. Joseph, P. Manimuthu, S. Sambasivam, S. N. Karthick, K. Vijayarangamuthu, A. Sendilkumar, K. Asokan, H. J. Kim, B. C. Choi, C. Venkateswaran, and R. Mohan, *Appl. Surf. Sci.* 284, 624 (2013).
[39] G. Sanal Kumar, N. Illyaskutty, S. Suresh, R. S. Sreedharan, V. U. Nayar, and V. P. M. Pillai, *J. Alloys Compd.* 698, 215 (2017).
[40] N. Illyaskutty, H. Kohler, T. Trautmann, M. Schwotzer, and V. P. M. Pillai, *J. Mater. Chem. C* 1, 3976 (2013).
[41] A. Chithambararaj, N. S. Sanjini, A. C. Bose, and S. Velmathi, *Catal. Sci. Technol.* 3, 1405 (2013).
[42] R. Choudhary and R. P. Chauhan, *J. Mater. Sci. Mater. Electron.* 27, 11674 (2016).
[43] O. Seo, O. Sakata, M. Kim, S. Hiroi, and C. Song, 253101 (2017).
[44] D. Nath, F. Singh, and R. Das, *Mater. Chem. Phys.* 239, 122021 (2020).
[45] V. Mote, Y. Purushotham, and B. Dole, *J. Theor. Appl. Phys.* 6, 2 (2012).
[46] A. Hepp and C. Baerlocher, *Aust. J. Phys.* 41, 229 (1988).
[47] N. C. Halder and C. N. J. Wagner, *Acta Crystallogr.* 20, 312 (1966).
[48] L. Motevalizadeh, Z. Heidary, and M. E. Abrishami, *Bull. Mater. Sci.* 37, 397 (2014).
[49] M. K. Hossain, A. A. Mortuza, S. K. Sen, M. K. Basher, and M. W. Ashraf, *Opt. - Int. J. Light Electron Opt.* 171, 507 (2018).
[50] R. Sivakami, S. Dhanuskodi, and R. Karvembu, 152, 43 (2016).
[51] H. Search, C. Journals, A. Contact, M. Iopscience, and I. P. Address, 2231 (2006).
[52] A. Chithambararaj, B. Winston, N. S. Sanjini, S. Velmathi, and A. C. Bose, 15, 4913 (2015).
[53] H. Search, C. Journals, A. Contact, M. Iopscience, and I. P. Address, 065305.
[54] P. S. Tamboli, C. V Jagtap, V. S. Kadam, R. V Ingle, R. S. Vhatkar, and S. S. Mahajan, *Appl. Phys. A* 0, 0 (2018).
[55] P. Wongkrua, T. Thongtem, and S. Thongtem, *J. Nanomater.* 2013 (2013).
[56] L. G. Pereira, L. E. B. Soledade, J. M. Ferreira, S. J. G. Lima, V. J. Fernandes, A. S. Araújo, C. A. Paskocimas, E. Longo, M. R. C. Santos, A. G. Souza, and I. M. G. Santos, *J. Alloys Compd.* 459, 377 (2008).
[57] A. B. Murphy, *Sol. Energy Mater. Sol. Cells* 91, 1326 (2007).

[58] A. Chithambararaj, N. S. Sanjini, S. Velmathi, and A. Chandra Bose, *Phys. Chem. Chem. Phys.* 15, 14761 (2013).
[59] G. P. Joshi, N. S. Saxena, R. Mangal, A. Mishra, and T. P. Sharma, *Bull. Mater. Sci.* 26, 387 (2003).
[60] D. Scirè, P. Procel, A. Gulino, O. Isabella, M. Zeman, and I. Crupi, *Nano Res.* 12 (2020).
[61] B. E. Sernelius, K. F. Berggren, Z. C. Jin, I. Hamberg, and C. G. Granqvist, *Phys. Rev. B* 37, 10244 (1988).
[62] Y. Kim, W. Lee, D. R. Jung, J. Kim, S. Nam, H. Kim, and B. Park, *Appl. Phys. Lett.* 96, 1 (2010).
[63] S. Yang, Y. Liu, T. Chen, W. Jin, T. Yang, M. Cao, S. Liu, J. Zhou, G. S. Zakharova, and W. Chen, *Appl. Surf. Sci.* 393, 377 (2017).
[64] H. Liu, Y. Cai, M. Han, S. Guo, M. Lin, M. Zhao, Y. Zhang, and D. Chi, *Nano Res.* 11, 1193 (2018).
[65] G. Horowitz, *J. Appl. Phys.* 118 (2015).
[66] N. Shimosako, Y. Inose, H. Satoh, K. Kinjo, T. Nakaoka, T. Oto, K. Kishino, and K. Ema, *J. Appl. Phys.* 118 (2015).
[67] M. B. Sreedhara, H. S. S. R. Matte, A. Govindaraj, and C. N. R. Rao, *Chem. - An Asian J.* 8, 2430 (2013).
[68] S. Ali and M. A. Farrukh, *J. Chinese Chem. Soc.* 65, 276 (2018).
[69] E. Burstein, *Phys. Rev.* 93, 632 (1954).
[70] Q. Zheng, J. Huang, S. Cao, and H. Gao, *J. Mater. Chem. C* 3, 7469 (2015).
[71] D. Xiang, C. Han, J. Zhang, and W. Chen, *Sci. Rep.* 4, 1 (2015).